Chapter 3

Similarities and differences in the ordering at short and long ranges in a $NaNbO_3$ based Pb-free smart system: A key to functional properties

3.1 Introduction

Crystallographic symmetry of the material is one of the important factors that influence various physical properties such as ferroelectricity, piezoelectricity, optical properties, etc. [87, 232, 233, 234]. The crystal structure of the material could be changed by external stimuli such as pressure, temperature, compositional engineering, etc [87, 90, 232, 233, 235]. Strategies such as microstructure modification and compositional engineering are used as tools to tailor various functional properties of the materials at room temperature [232, 233]. Moreover, phase boundary engineering has been utilized to optimize the piezoelectric properties of lead-free ceramics [46, 236].

ABO_3 perovskites attracted researchers due to their multifunctionality and various interesting physical properties such as ferroelectricity, piezoelectricity, pyroelectricity, etc. [27, 237, 238]. The two most important classes of perovskites having these properties are Alkali niobates and Alkaline earth titanates. The lead-free alkali niobates are known to have large piezoresponse and have evoked considerable interest as next-generation piezoceramics [18, 237]. In addition, they also find their application in high-density optical storage, enhancing nonlinear optical properties, as hologram recording materials, etc. [18, 170, 171, 172]. These materials have garnered significant interest due to their unique properties and high-temperature stability. On the other hand, Alkaline earth titanates and their derivatives are known to possess a high dielectric constant and find their application in fabricating various piezoelectric and piezoelectric devices [9, 239]. However, their temperature stability is poor as compared to Alkali niobates.

Sodium Niobate ($NaNbO_3$) is a member of the Alkali Niobates family and exhibits a series of complex phase transitions with temperature [6, 36, 69, 157, 162]. The room temperature structure of $NaNbO_3$ (NN) is orthorhombic with *Pbcm* space group [cell size: $(\approx \sqrt{2}a_p) \times (\approx \sqrt{2}b_p) \times 4c_p)$] having a compound tilt system $(a_0^- a_0^- c_0^+)_1^2 (a_0^- a_0^- c_0^-)_2^3 (a_0^- a_0^- c_0^+)_3^1$, where a_p,b_p, and c_p are the parameters of subcell [1] [63, 240, 241]. However, this antiferroelectric structure is very delicate and transforms into a ferroelectric phase with space group $Pmc2_1$ on the addition of dopants at A and/or B site or when subjected to a sufficient electric field [90, 163, 164]. The low-temperature structure of Sodium Niobate is ferroelectric (SG: *R3c*; cell size:$(\approx \sqrt{2}a_p) \times (\approx \sqrt{2}a_p) \times (\approx 2\sqrt{3}c_p)$), while on increasing temperature, it makes transition into **R** phase [SG: *Pbnm*; cell size: $(\approx \sqrt{2}a_p) \times (\approx \sqrt{2}b_p) \times 6c_p$], **S** phase [SG: *Pbnm*; cell size: $(\approx \sqrt{2}a_p) \times (\approx \sqrt{2}b_p) \times 12c_p$], **T1** phase [SG: *Cmcm*; cell size: $(\approx 2a_p) \times (\approx 2b_p) \times 2c_p$], **T2** phase [SG: *P4/mbm*; cell size:$\sqrt{2}a_p \times \sqrt{2}a_p \times c_p$]

[1]The tilt system is denoted using modified Glazer notation, where the three letters correspond to the x, y, and z axes. The superscript indicates in-phase tilting (represented by $'+'$) or out-of-phase tilting (represented by $'-'$) along that axis, while the subscript denotes the cationic displacement along that axis. Sodium niobate belongs to a compound tilt system formed by stacking two simple tilt systems along the [001] axis. This stacking results in a repeat period of 4-unit cells along the [001] axis.

and finally transform into a Cubic phase [SG: $Pm\bar{3}m$; cell size: $a_p \times a_p \times a_p$] [6]. On the other hand, Barium Titanate ($BaTiO_3$) is a classical ferroelectric material having a room temperature Tetragonal structure with space group *P4mm*. Owing to its high dielectric constant, it finds its application in multilayer chip capacitors, sensors, transducers, etc. [9]. Although Barium titanate-based materials have several advantageous properties, their low-temperature stability of piezoelectric properties has hindered their widespread use in technology. The study of the solid solution of Sodium niobate and Barium Titanate has been an area of significant interest [32, 35, 39, 39, 40, 41, 42, 242].

Abdelkefi et al. found that the NN-xBT compositions within a range of $x = 0.925$ to 0.45 showed relaxor behaviour at room temperature, attributing it to the presence of nanoscale heterogeneities, which results in a local disordered relaxor system [207]. Another report by Zeng et al. reported high ferroelectric and piezoelectric properties in NN-xBT, particularly for $x = 0.10$ [35]. However, both of these studies have limited information on the crystallographic aspects of the solid solution. Recently, Zuo et al. conducted a study on the structure of NN-xBT for the range of $0.15 \leq x \leq 0.25$ and discovered that despite a phase transition from tetragonal to cubic on an average scale, there is always a local tetragonal phase present regardless of the content of BT. This local distortion was caused by the competition between different local displacement directions of the B site Nb[001] and Ti[111], which ultimately disrupted the long-range ferroelectric order [40].

$PbTi_xZr_{1-x}O_3$ (PZT) is a widely used lead-based functional material in which the Morphotropic Phase Boundary (MPB) is stable for $0.48 \leq x \leq 0.50$ [21, 31]. It combines orthorhombic $PbZrO_3$ (antiferroelectric, SG: *Pbam*) and tetragonal $PbTiO_3$ (ferroelectric, SG: *P4mm*). To emulate a similar but lead-free system, we created a solid solution of $NaNbO_3$ (NN) with $Ba_{0.9}Ca_{0.1}TiO_3$ (BCT), which can induce inter-ferroelectric phase transitions leading to Morphotropic or Polymorphic phase boundary at room temperature. Sodium Niobate is characterized by an orthorhombic structure having a long-range antifer-

roelectric (AFE) ordering (SG: *Pbcm*) while exhibiting a local rhombohedral structure (SG: *R3c*). In contrast, $Ba_{0.9}Ca_{0.1}TiO_3$ exhibits a ferroelectric tetragonal structure with space group *P4mm*. It was found that in (Ba, Ca) TiO_3, Ca^{+2} cations become locally off-centred since they have smaller ionic radii than Ba^{+2} cations. Further, the ferroactive Ca^{+2} cations also promote the off-centring of the B site (Ti^{+4}) cation as Pb^{+2} does in $PbTiO_3$, leading to significant enhancement in ferroelectric polarization [202]. This makes $Ba_{0.9}Ca_{0.1}TiO_3$ (BCT) analogous to $PbTiO_3$ [38]. It is also reported that the inclusion of Ca at the Ba site in $BaTiO_3$ promotes finer grain size and stable ferroelectric domains, which results in high dielectric permittivity, low loss, and high polarization [243]. By varying the BCT content in NN matrix, various phases get stabilised having different ferroic ordering, *viz.,* antiferroelectric (i.e., *Pbcm*), ferroelectric (i.e., $Pmc2_1$, *Amm2*, *P4bm* & *P4mm*) and paraelectric (i.e., $Pm\bar{3}m$) along with regions where these phases coexist. A significant improvement in physical properties, such as dielectric permittivity and ferroelectric polarization, has been observed within the region where two ferroelectric phases coexist. This enhancement could be attributed to the presence of a large number of possible polarization orientations similar to widely reported lead-based systems, *viz.,* PZT. The compositions with higher BCT content, i.e., $x \geq 0.50$, have shown anomalous existence of two cubic phases. Moreover, we have observed slim ferroelectric hysteresis loops for these compositions, which have been attributed to the existence of polar nano regions within the paraelectric matrix. The coexistence of multiple phases and the presence of ferroelectric polarization within a long-range paraelectric structure hold significant technological significance and offer opportunities for developing various devices, such as sensors, transducers, ferroelectric memory, and energy storage devices.

3.2 Experimental

Samples with different composition of (1-x)$NaNbO_3$-$x$$Ba_{0.9}Ca_{0.1}TiO_3$ (NN-xBCT) in the range $0 \leq x \leq 1.0$ have been synthesized using conventional solid state reaction method. High purity precursor powder of Sodium niobate (Na_2CO_3), Barium carbonate ($BaCO_3$), Calcium carbonate ($CaCO_3$), Niobium pentaoxide (Nb_2O_5) and Titanium di-oxide (TiO_2) have been used as starting material. Firstly, all the raw materials were weighed according to composition stoichiometry, followed by Ball milling for 24 hours in an ethanol medium. After that, all the samples were calcined at 1000 °C for 5 hr in an air medium. Afterwards, all the samples were ball-milled and calcined again in similar conditions to rule out the presence of any non-reacted material or unwanted phase. The calcined powder was pressed using a uniaxial hydraulic press, and hence formed cylindrical pellets were sintered at 1100-1200 °C with a dwell time of 4 hr. The density of all sintered pellets was found to be in the range of 96–98 % of the theoretical density, which indicates that the samples were highly dense and well-sintered. The density was measured using the Archimedes method, which is a standard technique for determining the bulk density of ceramic materials. XRD patterns of the samples were collected after annealing the powder at 300-500 °C for 4 hours, after crushing the sintered pellets to remove the effect of residual stress incurred during the grinding. The powder X-ray diffraction data have been collected using a High-Resolution X-ray diffractometer (Rigaku SmartLab 9kW) with Cu K_α radiation. The X-ray diffraction data have been collected in the 2θ range of 20°-120° with a step size of 0.02°. The Room temperature Raman spectra have been collected using *alpha300 RAS* system from WiTec with an excitation source of 532 nm green laser. Silver electrodes were fired on the top and bottom surfaces of the samples for the subsequent electrical measurement. A Precision LC II ferroelectric tester (Radiant Technologies Inc.) was used to obtain the ferroelectric (P-E) loops. The temperature-dependent dielectric measurements were carried out using

a Keysight LCR meter in the heating mode with a ramping rate of 1.5 K/min. We have obtained the Scanning Electron Microscope (SEM) data from Nova Nano SEM 450.

3.3 Results And Discussion

The SEM images taken from the fractured surface of as-sintered pellets show well-formed grains with dense microstructure (see Fig. 3.1). The subsequent section provides an overview of the structural analysis of NN-xBCT.

3.3.1 High-resolution X-ray diffraction, Dielectric and Raman analysis for $0.00 \leq x \leq 0.25$

The composition-dependent X-ray diffraction patterns of (1-x) $NaNbO_3$ -x $Ba_{0.9}Ca_{0.1}TiO_3$ in the range $0 \leq x \leq 0.25$ have been shown in Fig. 3.2. Although the X-ray data have been collected in the 2θ range of 20°-120°, we have shown a limited range for a clear display of peak positions and intensity. All the samples have a pure phase, and we have not observed the presence of any impurity within the detection limit of the diffractometer. The diffraction patterns of all the compositions have been indexed with respect to a doubled pseudocubic cell $2a_p \times 2b_p \times 2c_p$. The diffraction patterns of perovskite materials are often characterized by the presence of superlattice reflections, which arise from the tilting of the oxygen octahedra. These tilts result in a multipling of the pseudocubic cell, and the indices of the superlattice reflections are therefore defined with respect to the doubled pseudocubic cell [58, 59]. In the above convention, the superlattice reflections are represented by at least one odd integer [58, 59]. To provide visual clarity, a magnified view of superlattice reflections and main perovskite reflections has been shown in Fig. 3.3. The reflections marked as I_1, Q, O, C, and I_2 are superlattice reflections, while M is a main perovskite reflection (see Fig. 3.3(a)) [72]. The (ooe), (ooo), and half-integrated type reflections are

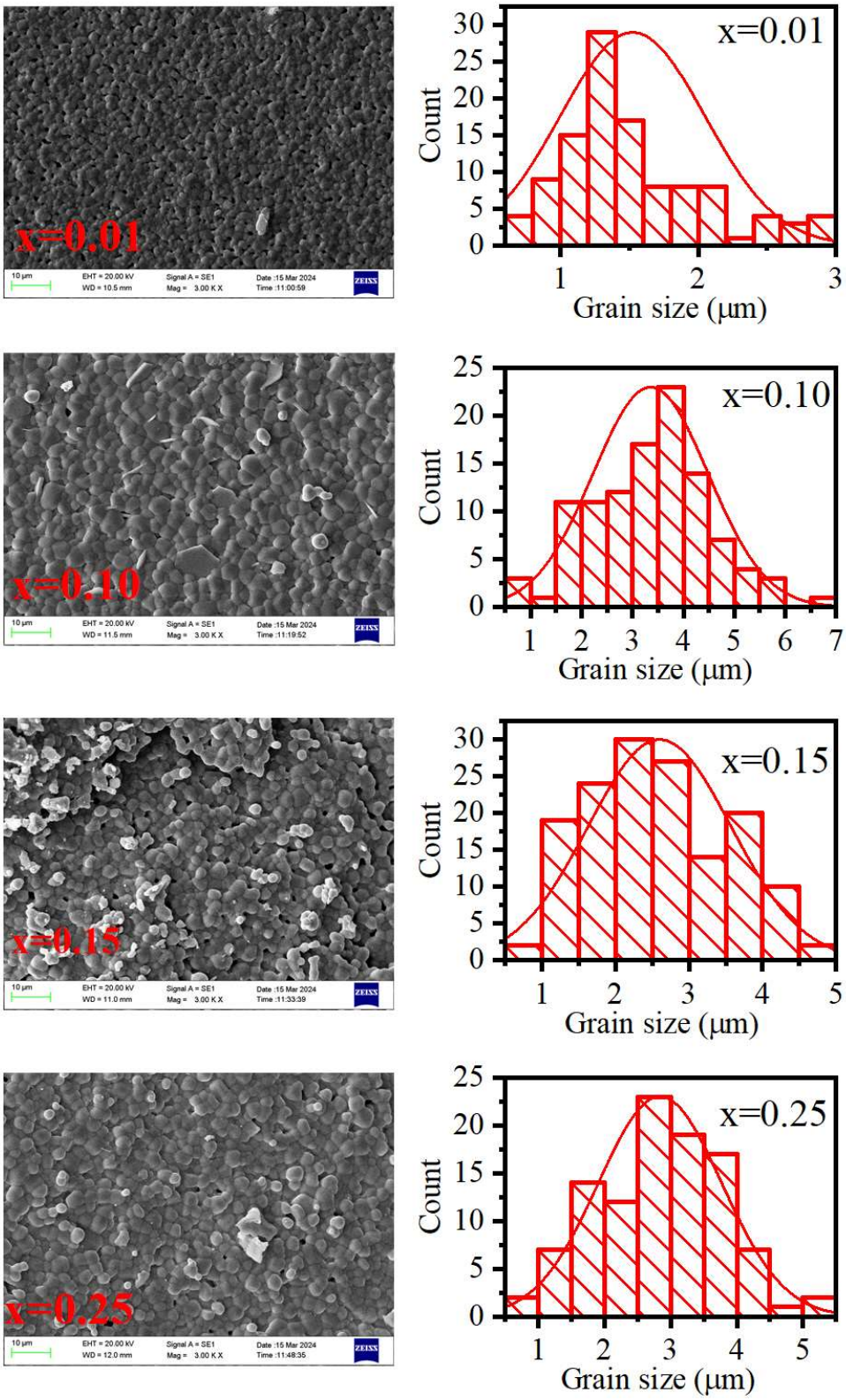

Fig. 3.1 Scanning electron micrographs and grain size distribution plots of the sintered pellets of NN-*x*BCT ceramics for x= 0.01, 0.10, 0.15, and 0.25.

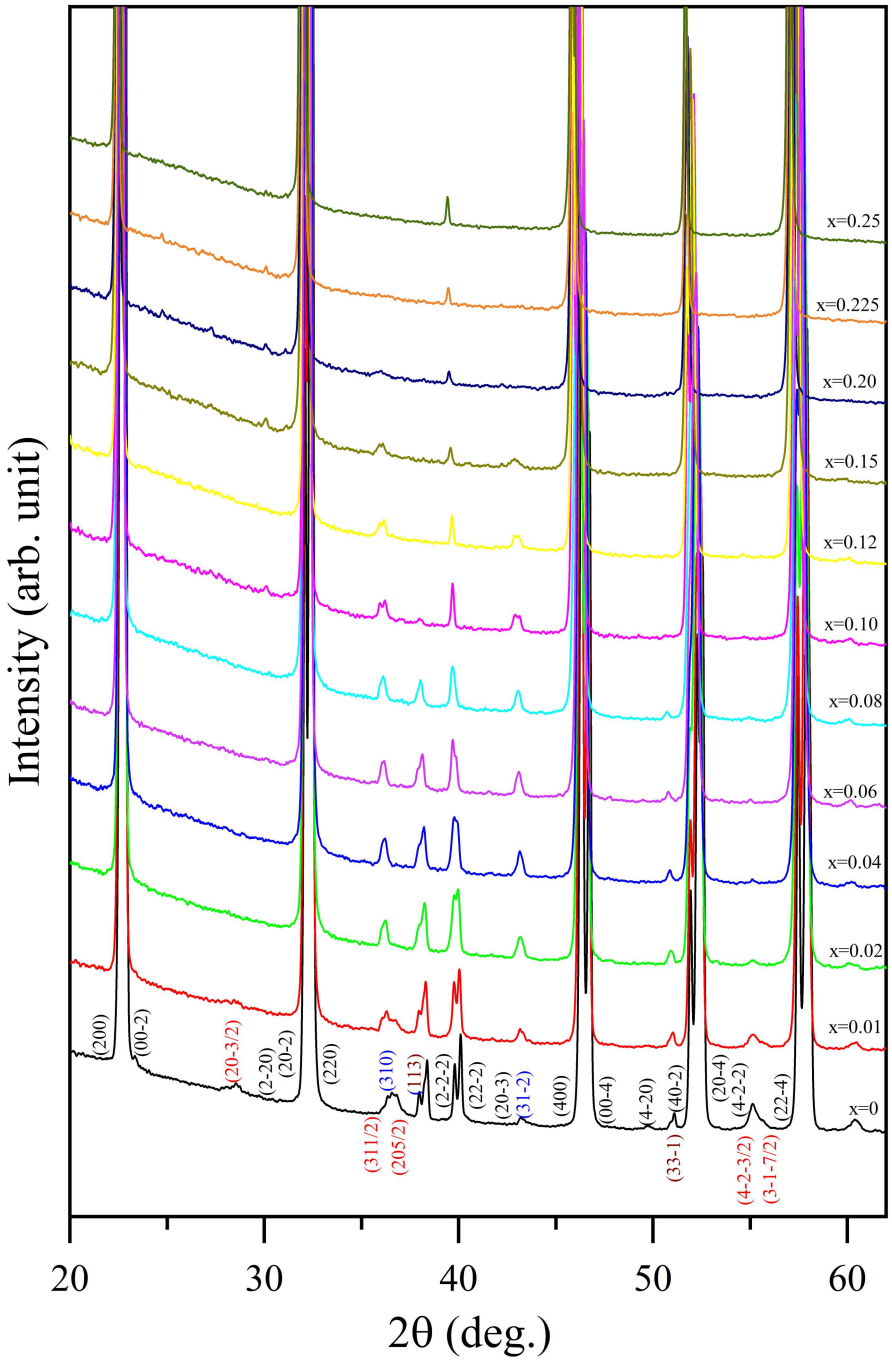

Fig. 3.2 Composition dependent powder X-ray diffraction profile of NN-xBCT for $0.00 \leq x \leq 0.25$. The Bragg reflections have been indexed with respect to a doubled perovskite cell.

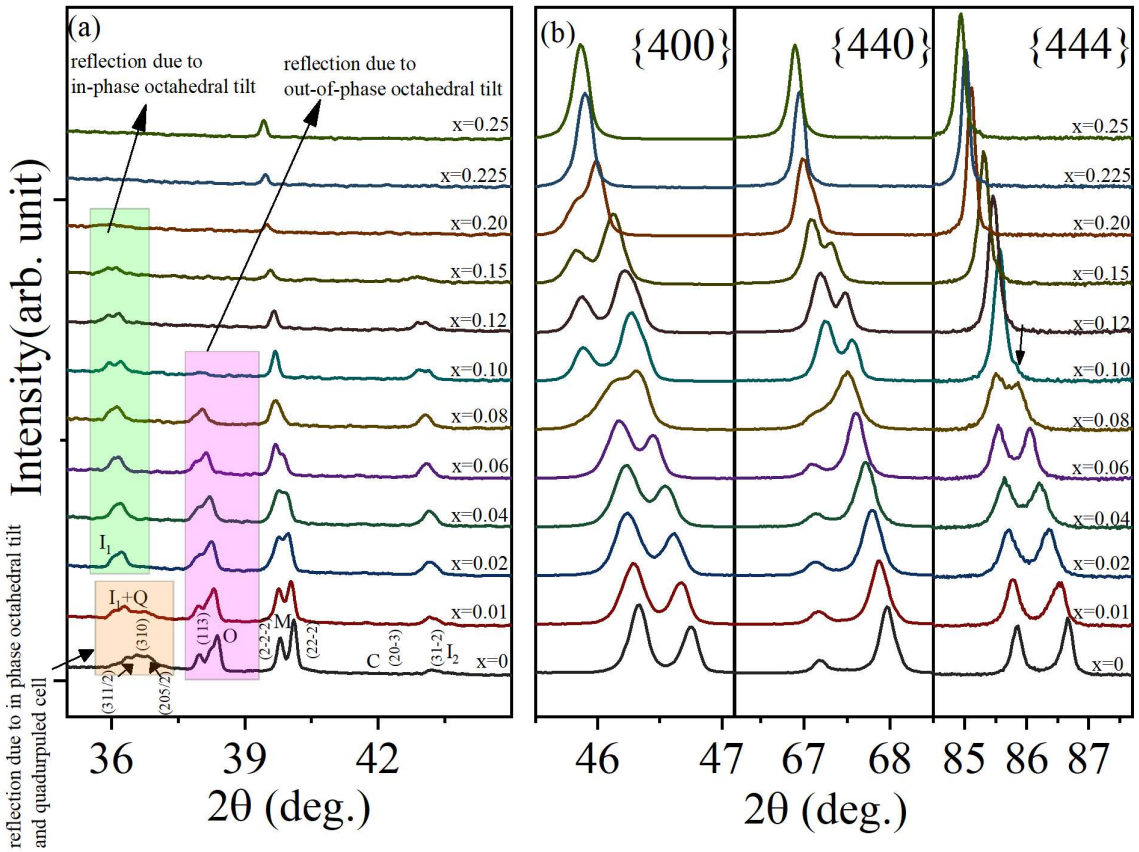

Fig. 3.3 Evolution of superlattice reflections(left panel) and main perovskite reflections(right panel) with increasing BCT content.

representative of in-phase octahedral tilt, out-of-phase octahedral tilt, and quadrupling of the unit cell. These features are linked with phonon condensation at M (q = 1/2,1/2,0), R (q = 1/2,1/2,1/2), and T (q = 1/2,1/2,1/4) points of the cubic brillouin zone, respectively. The reflection (I_1+ Q) comprised of odd-odd-even(ooe) and half-integered type indices for x=0 and x=0.01, while it has only (ooe) type indices(I_1) for compositions $0.02 \leq x \leq 0.20$. Further, the superlattice reflections O and I_1 have (ooo) and (ooe) type indices, respectively. The C reflection has (oee) type indices, which correspond to the anti-parallel displacements of the A-site cation. The composition with x=0 corresponds to pure Sodium Niobate ($NaNbO_3$) having an antiferroelectric orthorhombic structure at room temperature, with space group (SG: *Pbcm*) and cell size $(\approx \sqrt{2}a_p) \times (\approx \sqrt{2}b_p) \times 4c_p$. The quadrupling of a unit cell along one crystallographic axis is reflected in the diffraction pattern by the presence of reflections possessing half-integer indices (reflection marked as Q). On doping with BCT, drastic changes have been seen in the diffraction patterns. The intensities of superlattice peaks vary in the following manner:(i) The half-integer type indices vanish for $x \geq 0.02$. (ii) The intensity of ooo-type reflection decreases with increasing x and vanishes for x>0.10. (iii) The intensity of the ooe-type reflections decreases gradually with x, but they last up to x=0.20. For $x > 0.20$, superlattice reflections are not visible. In contrast to the superlattice reflections, the main perovskite reflections represent the symmetry of the elementary cell. Fig. 3.3(b) depicts the evolution of the main perovskite reflections with increasing BCT content in the NN matrix. The main perovskite reflections *viz.,* {400}, {440}, and {444} for all the compositions are positioned around 45°, 66° and 85°. The doublet nature of {hhh} type reflections corresponding to a basic cell is representative of a pseudo-monoclinic symmetry of the orthorhombic supercell. It can be seen clearly in Fig. 3.3(b) that the {444} doublet transforms into a singlet for $x > 0.08$. The transformation from doublet to singlet (of {hhh} reflection) suggests a transition from a pseudo-monoclinic to an orthogonal system of the elementary cell. Other than

that, the {h00} reflections show a peak reversal around $x = 0.08$, suggesting a structural phase transition. Finally, above $x = 0.20$, all the peaks become singlets, and the system transforms into a long-range cubic phase as depicted in the XRD pattern. To explore the composition-dependent phase diagram, Rietveld refinements of all the diffraction patterns have been carried out using the FULLPROF package. The background was described in terms of linear interpolation between set background points of refinable heights. The refined parameters include the zero point of the detector, unit cell parameters, atomic coordinates, thermal parameters, peak shape parameters, etc. For the sake of consistency, we have carried out sequential refinement, i.e., for higher composition, we have used refined parameters of lower composition as initial parameters.

In order to fit the diffraction pattern of pure Sodium Niobate($NaNbO_3$; NN) (x=0), we have used the widely reported orthorhombic structure with the *Pbcm* space group. This model fits very well with the diffraction pattern of NN. For x=0.01, drastic changes occur, particularly around quadrupled peaks at around 37°. We tried to fit the diffraction pattern of x=0.01 with the same *Pbcm* model. However, this model does not give a satisfactory fit. In particular, the *Pbcm* model fails to account for the changed width of the I_1+ Q (around 37°). It has been seen earlier that the antiferroelectric *Pbcm* phase of NN is very delicate and transforms into a ferroelectric phase on a small amount of doping or applying a sufficient electric field [90, 163, 164]. Furthermore, the presence of superlattice reflection at 37° (indices marked as Q) rules out the complete transformation of the *Pbcm* phase into another phase. Due to this, we suspect an additional phase that coexists with the antiferroelectric *Pbcm* phase. This additional phase can most likely be a ferroelectric phase $Pmc2_1$ (tilt system: $a^-_+a^-_+c^+_0$, cell size: $2a_p \times \sqrt{2}b_p \times \sqrt{2}c_p$) since it has been reported earlier in Li substituted sodium niobate [90]. In light of the literature, we have tried a two-phase model *Pbcm*+ $Pmc2_1$ for $x = 0.01$. This model accounted very well and gives a satisfactory fit to the diffraction pattern. The phase fractions of *Pbcm* and $Pmc2_1$ phases for

this composition are 34% and 66%, respectively. The intensity of the characteristic AFE reflections disappears for $x \geq 0.02$, which marks the transformation of the AFE(*Pbcm*) phase into the FE($Pmc2_1$) phase. Thereafter, a single $Pmc2_1$ phase was sufficient to fit the diffraction pattern of $x = 0.02$, 0.04, and 0.06. However, for $x = 0.08$ and above, drastic changes occur in the diffraction patterns, which include suppression of the superlattice reflections related to in-phase tilting of octahedra and doublet to singlet transition of {hhh} type reflections. The singlet nature of {444} reflection indicates that the new phase has a pure orthorhombic or tetragonal nature rather than pseudo-monoclinic at the elementary level. We have considered the following models to fit the structure of composition $x = 0.10$ consistent with the literature (i) $Pmc2_1$ (ii) *P4bm* (iii) *Amm2* (iv) *P4bm* +$Pmc2_1$ (v) $Pmc2_1$+ *Amm2*. Here, the phases *Amm2* and *P4bm* have tilt systems $a_0^+b_0^0c_+^0$ and $a_0^0a_0^0c_+^+$, respectively. In addition, the phase considerations have also been taken into account on the basis of a list of space groups derived by combining various irreducible representations in the isotropy software [244]. A single-phase *P4bm* or *Amm2* models were found to be insufficient due to the presence of O superlattice reflection, which is related to the out-of-phase rotation of oxygen octahedra. The model (v) gives the best fit to the diffraction pattern for compositions $x = 0.08$, 0.10. The refined parameters with the *Amm2* + $Pmc2_1$ model are shown in Table 3.2. Upon increasing the BCT content, the compositions $x = 0.12$ and 0.15 could be fitted using a single *Amm2* model due to the absence of superlattice reflections corresponding to out-of-phase octahedral rotation. The tetragonal *P4bm* model was used to fit the diffraction pattern of $x = 0.20$. For the composition $x = 0.25$, the absence of the superlattice peaks and the singlet nature of the main perovskite reflections suggest that the structure has been transformed into a cubic phase. Hence, we used a Cubic $Pm\bar{3}m$ model to fit the diffraction and obtained a satisfactory fit (see Fig. 3.4).

Fig. 3.5 shows the composition-dependent evolution of elementary cell parameters, volume, and monoclinic angle obtained from Rietveld refinements. To obtain the monoclinic

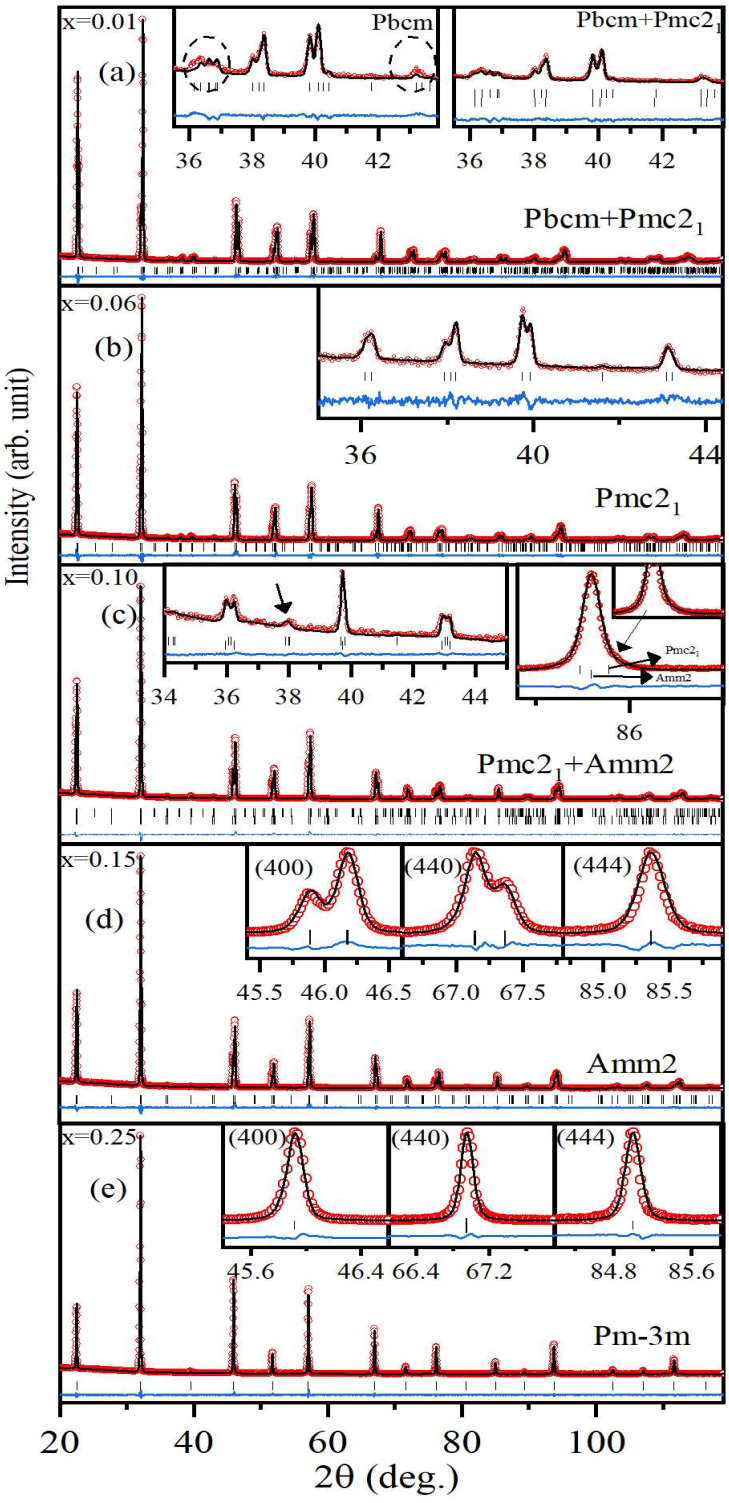

Fig. 3.4 Rietveld refined X-ray diffraction (XRD) patterns of NN-xBCT for a few representative compositions.

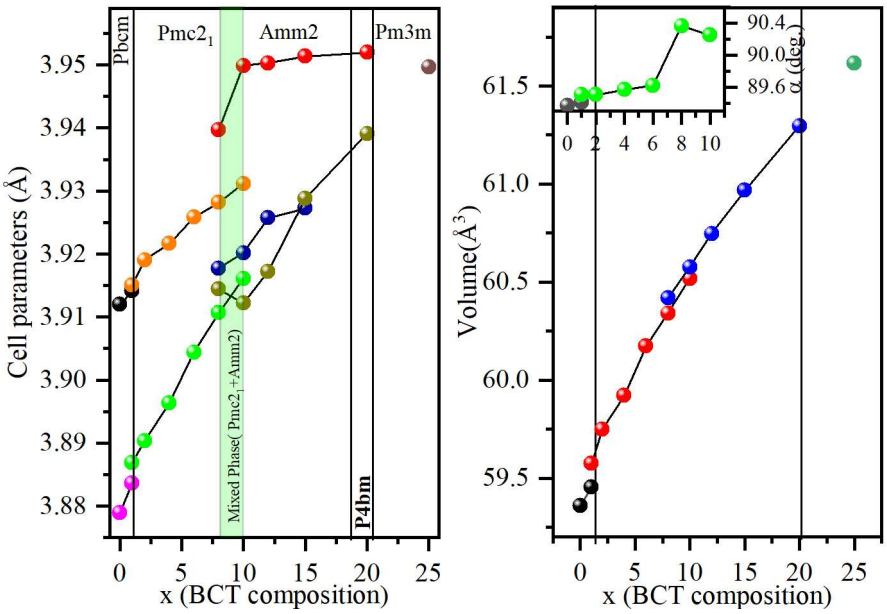

Fig. 3.5 Variation of (a) lattice parameters, (b) volume of the elementary cell. (Inset shows the evolution of monoclinic angle for composition with pseudo-monoclinic basic cell).

Table 3.1 Structural parameters, phase fraction, and various agreement factors obtained from the Rietveld refinements of the X-ray diffraction patterns for x=0.01 via two-phase (*Pbcm*+*Pmc2$_1$*) coexistence model.

	Space group: *Pbcm*				Space group: *Pmc2$_1$*			
Atoms	*x*	*y*	*z*	U(Å^2)	*x*	*y*	*z*	U(Å^2)
Na1/Ba1/Ca1	0.239(2)	0.2500	0.000	0.012(5)	0.000	0.238(6)	0.736(7)	0.015(8)
Na2/Ba2/Ca2	0.240(2)	0.2270(18)	0.25	0.017(5)	0.500	0.244(7)	0.753(7)	0.009(7)
Nb/Ti	0.2548(5)	0.7386(2)	0.1246(2)	0.0076(6)	0.7504(9)	0.7463(8)	0.766(6)	0.0032(8)
O1	0.676(4)	0.250	0.000	0.012(6)	0.000	0.223(8)	0.295(9)	0.004(12)
O2	0.193(4)	0.731(2)	0.250	0.005(5)	0.500	0.285(7)	0.300(8)	0.001(11)
O3	0.4760(14)	0.4479(18)	0.1431(8)	0.006(3)	0.232(3)	0.564(3)	0.059(4)	0.003(5)
O4	0.0271(16)	0.0115(19)	0.1131(10)	0.011(3)	0.297(3)	0.977(4)	0.48784	0.029(7)
	a=5.5066(1) Å, *b*=5.5644(1) Å, *c*=15.5348(2) Å				*a*=7.7736(2) Å, *b*=5.5127(2) Å, *c*=5.5603(2) Å			
	V= 475.953 Å^3, fraction=60.31%				*V*= 238.293 Å^3, fraction=39.69%			
	Agreement factors: R_{wp}=4.49, R_{exp}=3.10, χ^2=2.09							

Table 3.2 Structural parameters, phase fraction, and various agreement factors obtained from the Rietveld refinements of the X-ray diffraction patterns for x=0.10 via two-phase ($Pmc2_1$+ $Amm2$) coexistence model.

	Space group: $Pmc2_1$				Space group: $Amm2$			
Atoms	x	y	z	U(Å^2)	x	y	z	U(Å^2)
Na1/Ba1/Ca1	0.000	0.244(5)	0.764(13)	0.005(10)	0.000	0.7622(6)	0.003(9)	0.0039(7)
Na2/Ba2/Ca2	0.500	0.255(4)	0.737(11)	0.014(11)	-	-	-	-
Nb1/Ti1	0.749(3)	0.7485(13)	0.784(9)	0.0145(8)	0.500	0.000	0.76320(7)	0.0031(13)
Nb2/Ti2	-	-	-	-	0.500	0.500	0.25023	0.0009(12)
O1	0.000	0.221(13)	0.356(18)	0.01(3)	0.000	0.000	0.269(11)	0.002(5)
O2	0.500	0.300(11)	0.343(18)	0.01(3)	0.000	0.500	0.214(9)	0.008(6)
O3	0.239(6)	0.599(4)	0.116(10)	0.004(11)	0.500	0.751(7)	0.247(9)	0.0204(16)
O4	0.253(8)	0.993(8)	0.52542	0.008(12)	0.500	0.000	0.006(8)	0.019(5)
O5	-	-	-	-	0.500	0.500	0.00577	0.023(5)
	a=7.8325(4), b=5.5715(3) Å, c=5.5477(3) Å				a=3.9203(0) Å, b=7.9001(1) Å, c=7.8247(1) Å			
	V=242.09 Å^3, fraction=26.83%				V=242.34 Å^3, fraction=73.17%			
	Agreement factors: R_{wp}= 5.17, R_{exp}= 3.45, χ^2= 2.24							

cell parameters and angle, we have used the formula given in the literature [72, 76, 87]. The volume of the elementary cell increases by increasing the BCT content, since the unit cell volume of ($Ba_{0.9}Ca_{0.1}TiO_3$) is larger than $NaNbO_3$. Furthermore, the volume evolution in the solid solution (1-x)NN-xBCT does not follow Vegard's law, displaying a non-linear increase.

Ferroelectric and Dielectric Properties:

To quantify the ferroelectric properties of NN-xBCT, we have measured P-E hysteresis loop for a few selected compositions at Room temperature (see Fig. 3.6). All the P-E loops were measured at a field of 25 KV/cm at a measuring frequency of 10 Hz. From the hysteresis curves, it was noted that the remnant polarization of the samples exhibits a gradual increase until it reaches its maximum value at x = 0.10, which corresponds to a phase coexistence region. However, upon further increasing the BCT content beyond this point, the remnant polarization decreases. Notably, the remanent polarization experiences a three-fold increase as compared to the composition located off-boundary. This significant enhancement can be attributed to the coexistence of two ferroelectric phases ($Pmc2_1$+$Amm2$) at Room temperature. Here, P-E loops could be very well correlated

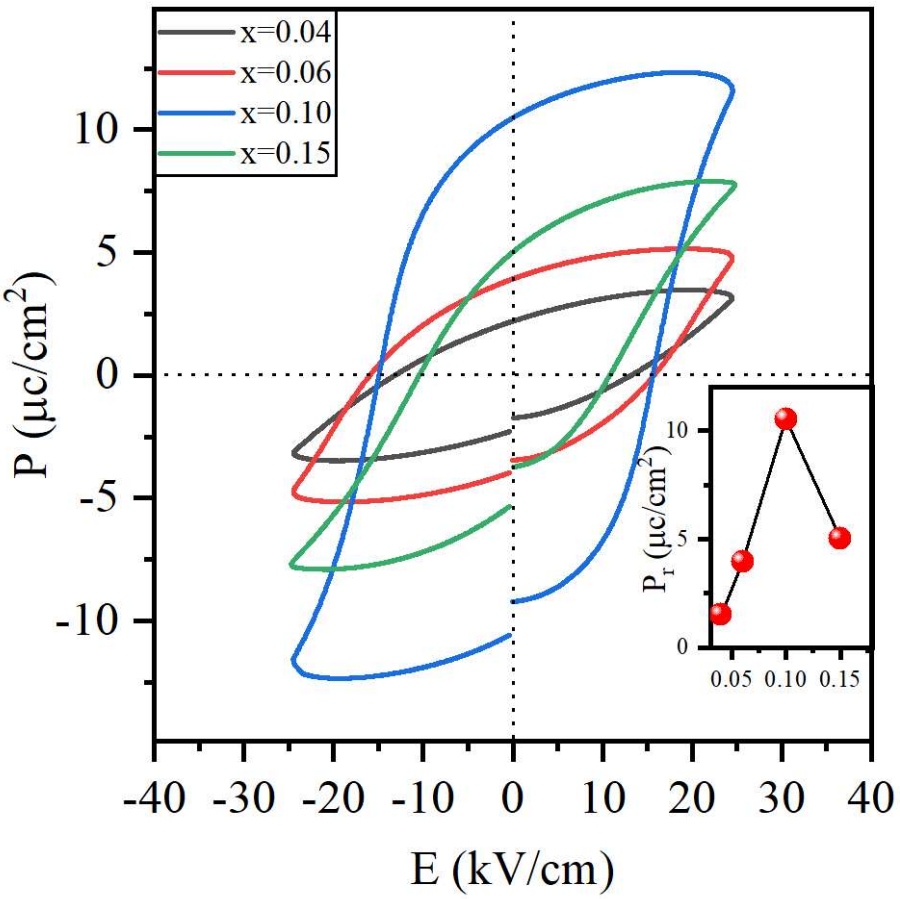

Fig. 3.6 Polarization vs Electric field(P-E) for some representative composition at 25 kV/cm and at a frequency of 10 Hz. The inset shows the remanent polarization as a function of composition.

with the off-centred displacements of the atoms/ions with respect to their centrosymmetric positions in the high symmetry cubic phase with $Pm\bar{3}m$ space group. The high polarization observed for $x = 0.10$ results from the cumulative effect of the dipole moments generated by off-centring of ferroactive cations. The displacement pattern of cations results in two coexisting ferroelectric phases *viz.*, $Pmc2_1$ and *Amm2*. The reduction in remanent polarization observed for $x > 0.10$ can be attributed to a reduced ferroelectricity content as the system approaches a high symmetry cubic structure for higher BCT content.

The variation of room temperature real and imaginary parts of the dielectric permittivity as a function of composition is shown in Fig. 3.7. The real part of dielectric permittivity

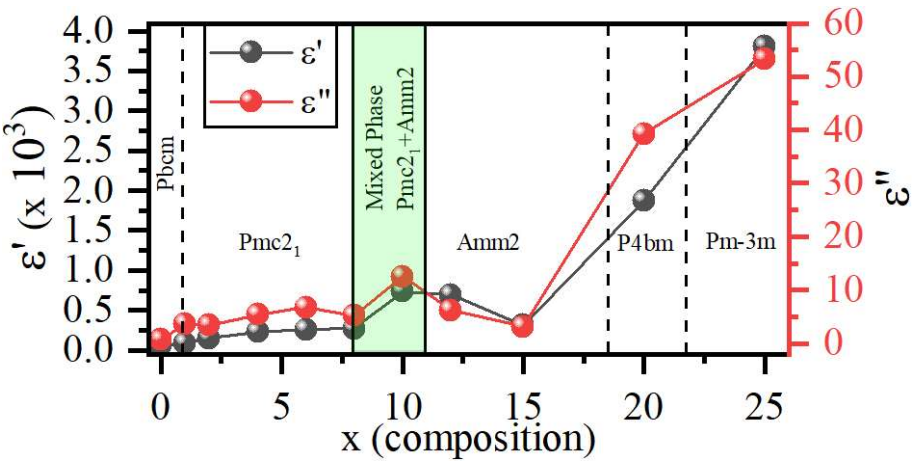

Fig. 3.7 Composition-dependent real and imaginary part of dielectric permittivity measured at 10 kHz.

increases by increasing the BCT content in the Sodium Niobate(NN) matrix. Both the real part (ε') and the imaginary part (ε") exhibit an intriguing anomaly around the composition $x = 0.10$. This particular composition corresponds to the presence of coexisting ferroelectric phases, *viz.*, *Pmc2$_1$* and *Amm2*, as confirmed by X-ray diffraction analysis. A sudden increase in ε' and ε" have been seen for $x \geq 0.20$. To investigate this anomalous increase, we have performed temperature-dependent dielectric analysis for $x = 0.25$. Fig. 3.8 shows the real part of dielectric permittivity in the temperature range of 100 K - 650 K at 10 kHz. Inset Fig. 3.8(a) shows the frequency dependence of maxima of the real part of dielectric permittivity at different frequencies in the range 1 kHz- 1 MHz. A very weak frequency-dependent dielectric maximum, which is a characteristic of diffuse type phase transition, has been observed. It is important to note that the maxima of the dielectric permittivity for this particular composition are positioned near room temperature. The sudden rise in the dielectric permittivity at room temperature for compositions $x \geq 0.20$ could be attributed to the presence of para-to-ferro phase transition near room temperature, as depicted in Fig. 3.7.

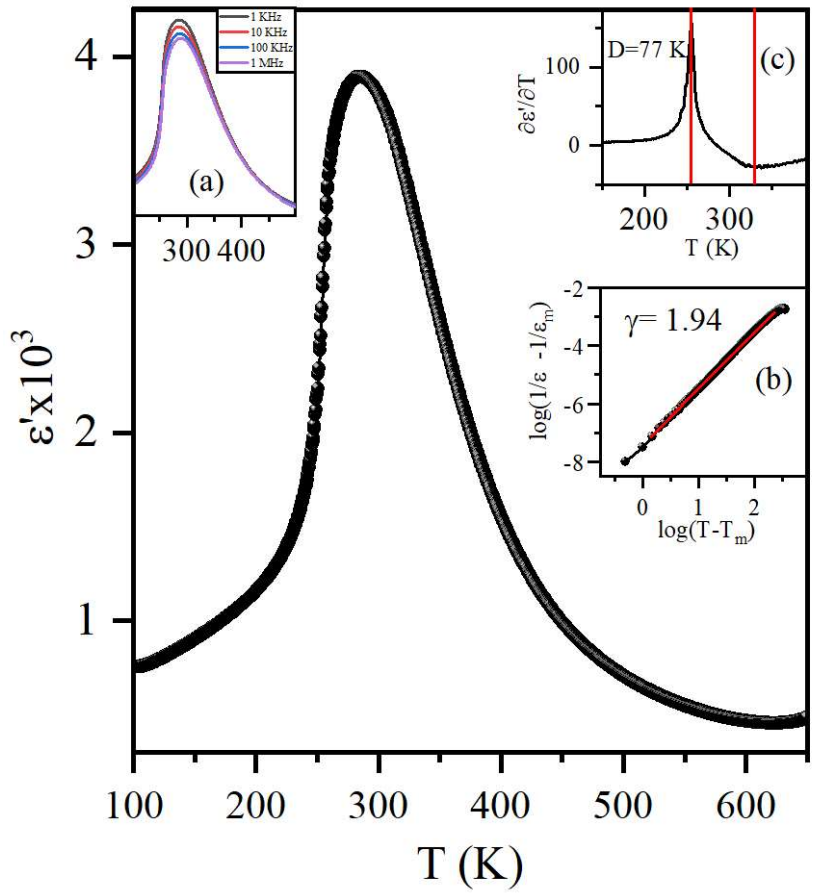

Fig. 3.8 Temperature dependent real part of dielectric permittivity for $x = 0.25$ at 10 kHz (a) frequency dependence of real part of dielectric permittivity (b) fitting of modified Curie-Weiss law (c) Diffusivity.

The diffuse phase transitions in the ferroelectric materials have been characterized using a modified Curie-Weiss law given by

$$\frac{1}{\varepsilon'} - \frac{1}{\varepsilon'_m} = \frac{[T - T_m]^\gamma}{C} \tag{3.1}$$

where T_m is the temperature corresponding to dielectric maximum, ε'_m is the real part of dielectric permittivity at T_m, γ is a critical exponent whose values lie between 1 and 2 (1 for classical ferroelectric material and 2 for pure relaxor material)[245]. For the composition $x = 0.25$, we employed the modified Curie-Weiss law to perform a fitting for the real part of

the dielectric permittivity. The outcome of this fitting is presented in Fig. 3.8(b). Notably, the calculated value for γ for this specific composition is determined to be 1.94. This value closely aligns with those found in relaxor ferroelectric materials. In spite of having such a high value of γ, the peak corresponding to dielectric maximum x = 0.25 shows very weak frequency dependence, which is a peculiar feature of materials with diffused phase transitions. Another important parameter to study the diffuseness of the permittivity peak is the degree of diffuseness (D), which can be calculated as [246],

$$D = T_{(\frac{d\varepsilon}{dT})_{min}} - T_{(\frac{d\varepsilon}{dT})_{max}} \tag{3.2}$$

A high degree of diffuseness(D=77 K) has been observed for x = 0.25 (see Fig. 3.8(c)). A weak frequency-dependent and highly diffuse dielectric peak near room temperature for x = 0.25 is an important feature that could be exploited for technological purposes.

Raman spectroscopic studies:

To gain a comprehensive understanding of the structural phase transitions occurring in the systems, it is important to supplement the information obtained from the diffraction technique with other techniques. Raman spectroscopy is sensitive to the local ordering and suitable for understanding the structural phase transitions in perovskite-based systems [223, 247, 248, 249]. Fig. 3.9 shows the Raman spectra for various compositions in the range 70-1000 cm^{-1}. All the Raman spectra are deconvoluted using a suitable number of Lorentz peaks. The Raman spectra of perovskites with the ABO_3 structure primarily result from two main factors: the motion of the A-site cation with respect to the BO_6 octahedra and the inherent vibrational(stretching and bending) modes of the oxygen octahedra. Following this, the Raman spectra of ABO_3 type perovskite can be divided into three regions: (i) Transnational modes: $\bar{\nu} < 150\ cm^{-1}$: (ii) Bending modes: $150 \leq \bar{\nu} \leq 450\ cm^{-1}$ (iii) stretching modes: $450 \leq \bar{\nu} \leq 850\ cm^{-1}$. Raman spectrum for x=0($NaNbO_3$)

is similar to what has been reported in literature [250, 251, 252]. We have calculated the number of expected Raman modes for the different phases of NN-xBCT using the online tool SAM available on the Bilbao Crystallographic server [253]. The Group theoretical analysis suggested 60, 57, 27, and 24 Raman active modes for *Pbcm*, *Pmc2$_1$*, *Amm2*, and *P4bm* phases of NN-xBCT. However, a total of 17, 15, and 12 peaks gave a sufficient fit to the Raman spectra of *Pbcm*, *Pmc2$_1$*, and *Amm2* phases, respectively. The number of calculated and fitted Raman modes may be different due to less resolved and broader features of the observed spectra. This broadening and overlapping of Raman modes can be attributed to the incorporation of different types of ions with distinct sizes at the A and B sites. The Raman vibration mode around 93 cm^{-1} is linked to the T-point instability of the cubic Brillouin zone, leading to a quadrupling of the unit cell [254]. This results in an antiferroelectric (AFE) phase (SG: *Pbcm*) of $NaNbO_3$ having a supercell (Unit cell size $\sqrt{2}a_p \times \sqrt{2}b_p \times 4c_p$). This mode disappears for $x > 0.01$, indicating transition of the AFE phase of $NaNbO_3$ (SG: *Pbcm*) into a ferroelectric phase with *Pmc2$_1$* space group. Additionally, the broad band around 150 cm^{-1} (observed for $0.08 \leq x \leq 0.15$) is indicative of a phase transition from a ferroelectric phase (FE1) with space group *Pmc2$_1$* (stable for $0.02 \leq x \leq 0.06$) to another ferroelectric phase (FE2) with space group *Amm2* (stable for $0.12 \leq x \leq 0.15$) via coexistence of the two ferroelectric phases (FE1+FE2) for $x = 0.08$ & 0.10. Moreover, for $x > 0.15$, the broad band around 150 cm^{-1} disappears, leaving only an asymmetric band around 220 cm^{-1}, marking a phase transition into another ferroelectric phase (FE3) with *P4bm* space group. Finally, the system transforms into a long-range cubic phase for $x > 0.20$, characterized by the appearance of four broad bands often attributed to the cationic disorder in the cubic matrix. Remarkably, Raman spectroscopy studies align with the crystallographic phases identified in the X-ray diffraction analysis, revealing a consistency between short and long-range ordering. The presence of the two coexisting

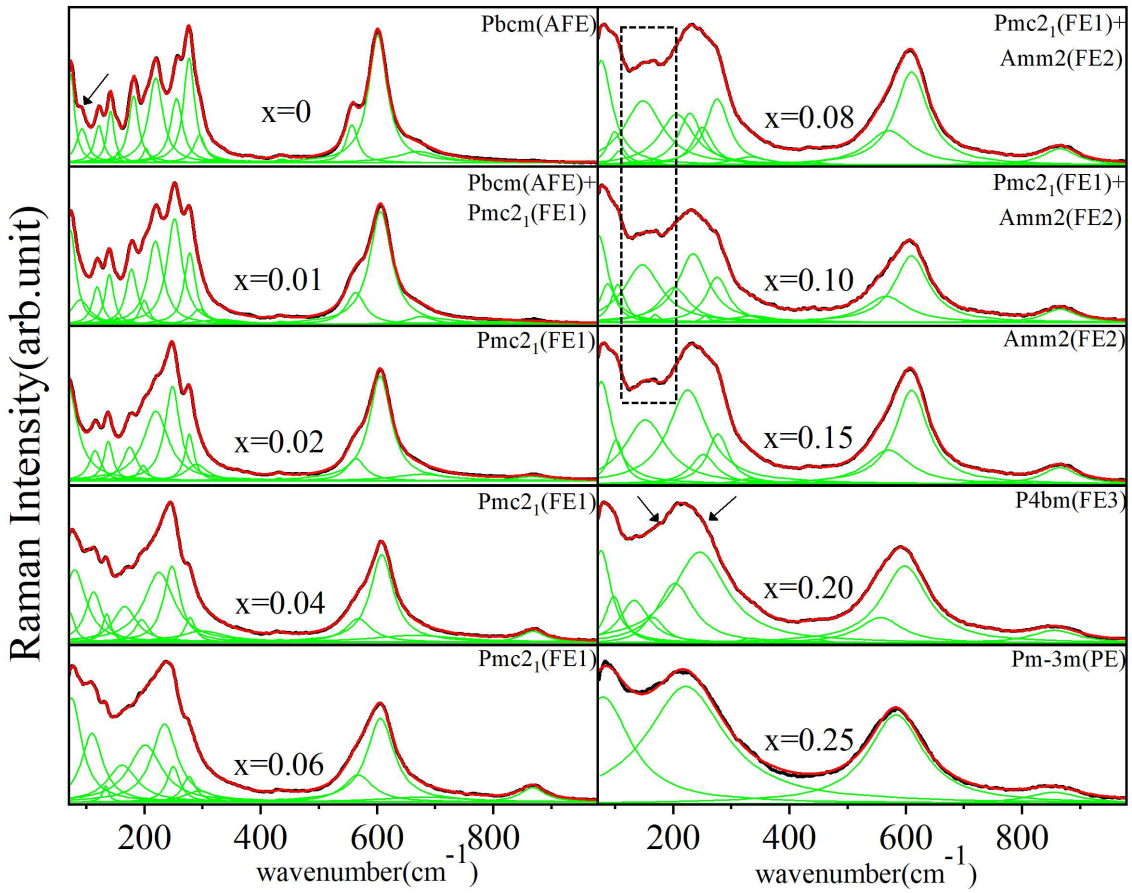

Fig. 3.9 Room temperature Raman spectra of NN-xBCT for different compositions. All the Raman spectra have been deconvoluted using a suitable number of Lorentz peaks. The Raman mode marked around 93 cm^{-1} for $x = 0$ (i.e., $NaNbO_3$) is linked to the T point instability of the cubic Brillouin zone. The appearance of a broad band around 150 cm^{-1} marks the phase transition *Pmc2$_1$* ($0.02 \leq x \leq 0.06$) $\rightarrow$ *Amm2* ($x = 0.15$) via coexistence of two ferroelectric phases for $x = 0.08$ & 0.10. This band disappears for $x > 0.15$, indicating another phase transition to *P4bm*.

phases revealed from X-ray diffraction analysis for $x = 0.01$(*Pbcm*+*Pmc2$_1$*) and $x = 0.08$, 0.10(*Pmc2$_1$*+*Amm2*) is clearly evident from the Raman analysis.

3.3.2 Studies on NN-*x*BCT for $0.30 \leq x \leq 1.0$: High resolution diffraction, Dielectric, and Raman spectroscopic analysis:

Fig. 3.10 depicts the High-resolution X-ray powder diffraction (HR-XRD) profiles for $\{200\}_{pc}$, $\{220\}_{pc}$, and $\{222\}_{pc}$ perovskite reflections for various compositions of NN-xBCT in the composition range of $0.30 \leq x \leq 1.0$. The distinct change in the Bragg reflections indicates a structural phase transition induced by the composition. The diffraction patterns for $x = 0.30$ and $x = 0.40$ are similar to that of $x = 0.25$ (i.e., all the pseudocubic reflections are singlets), suggesting a long-range cubic structure for the two compositions. Moreover, an additional shoulder starts to grow at the lower angles for some of the reflections, which is clearly evident for $\{200\}_{pc}$, $\{220\}_{pc}$, and $\{222\}_{pc}$ (see Fig. 3.10). For $x = 1.00$, i.e., $Ba_{0.9}Ca_{0.1}TiO_3$, the splitting of main perovskite peaks suggests a tetragonal structure in line with the literature [37]. Next, we aim to fix the structural model for the composition $0.50 \leq x \leq 0.90$. From the preliminary analysis of the characteristic reflections, it is obvious that a single cubic model will not be sufficient to fit the diffraction pattern of these compositions, and hence, we require an additional phase. To fix this additional phase, we have explored various plausible structural models, *viz.,* $Pm\bar{3}m$, *P4mm*, *R3m*, and mixed-phase models.

Fig. 3.11 illustrates temperature-dependent dielectric measurements for a few representative compositions. All the shown compositions *viz.,* $x = 0.40$, 0.60, and 0.80 exhibit diffused dielectric maxima showing strong frequency dependence. The frequency-dependent dielectric maxima are characteristic of relaxors originating from polar nanoregions [131, 255, 256]. Unlike typical ferroelectrics, the dielectric maxima, in the case of relaxors such as Pb(Mg, Nb)O_3(PMN), are not linked to a long-range phase transition

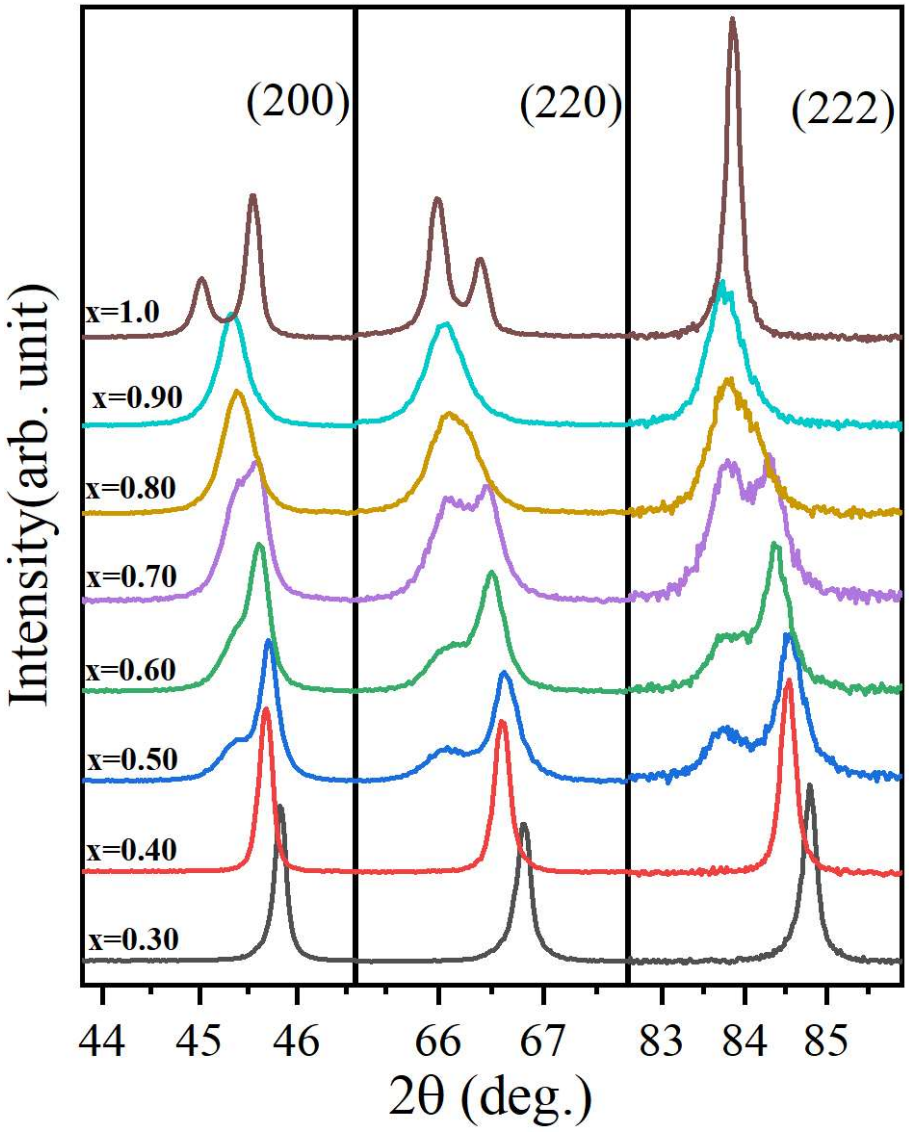

Fig. 3.10 Composition-dependent evolution of X-ray diffraction profiles of $\{200\}_{pc}$, $\{220\}_{pc}$, and $\{222\}_{pc}$ perovskite reflections of NN-xBCT for $0.30 \leq x \leq 1.0$.

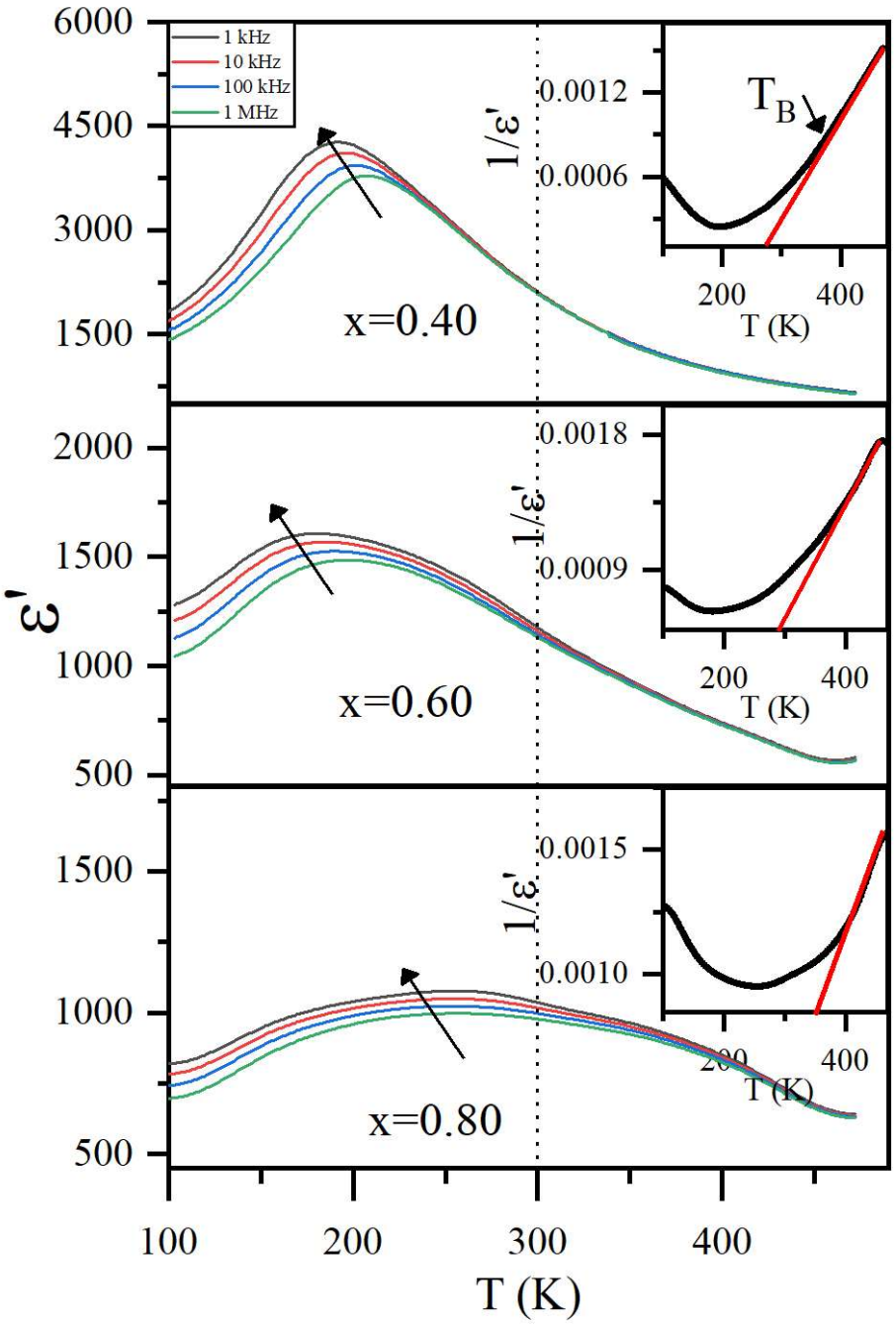

Fig. 3.11 Temperature dependent dielectric permittivity of NN-xBCT ceramics at several frequencies for x = 0.40, 0.60, and 0.80.

[131]. However, the application of a sufficient electric field can induce a ferroelectric phase [257]. On the other hand, in certain relaxor materials, a spontaneous transition from a paraelectric to a ferroelectric state occurs at low temperatures (for e.g., Pb(Mg, Nb)O_3(PMN)-$PbTiO_3$(PT)) [258]. The diffuseness of the dielectric maxima increases with increasing BCT content, which can be attributed to increased disorder due to differences between the size and oxidation states of cations at the A and B sites. In the insets of Fig. 3.11, the inverse dielectric permittivity versus temperature is plotted. A linear trend is observed well above the dielectric maximum temperature, and the point where the curve deviates from linearity is identified as the Burns temperature (T_B) [128]. Following the literature, the Burns temperature represents the onset of dynamic polar nanoregions (PNRs), usually characterized by a local symmetry distinct from the symmetry at the long ranges. The polar nanoregions (PNRs) nucleate below T_B, and their size grows with the decrease in temperature [130]. Although polar nanoregions (PNRs) contribute to the diffraction pattern in the form of diffuse scattering, their existence results in discrepancies in intensity during the Rietveld refinement process [134, 259, 260]. However, it is important to note that no long-range ferroelectric ordering exists in the relaxors above the temperature corresponding to dielectric maxima. Given that the dielectric maxima occur below room temperature for all the compositions with $0.50 \leq x \leq 0.80$, the probability of a long-range ferroelectric structure at room temperature appears unlikely.

In order to confirm the crystal structure for $x \geq 0.30$, we have performed the Le-bail refinements of all the synthesized compositions using different plausible models. The refined parameters include the zero point of the detector, background fitted by linear interpolation between a set of background points with refinable heights, lattice parameters, peak shape parameters, etc. The pseudo-voigt function was used to model the peak profile of Bragg reflections. The Rietveld refinement plots of the representative compositions have been included in the supplementary file. For x = 0.30 & 0.40, we have used a single

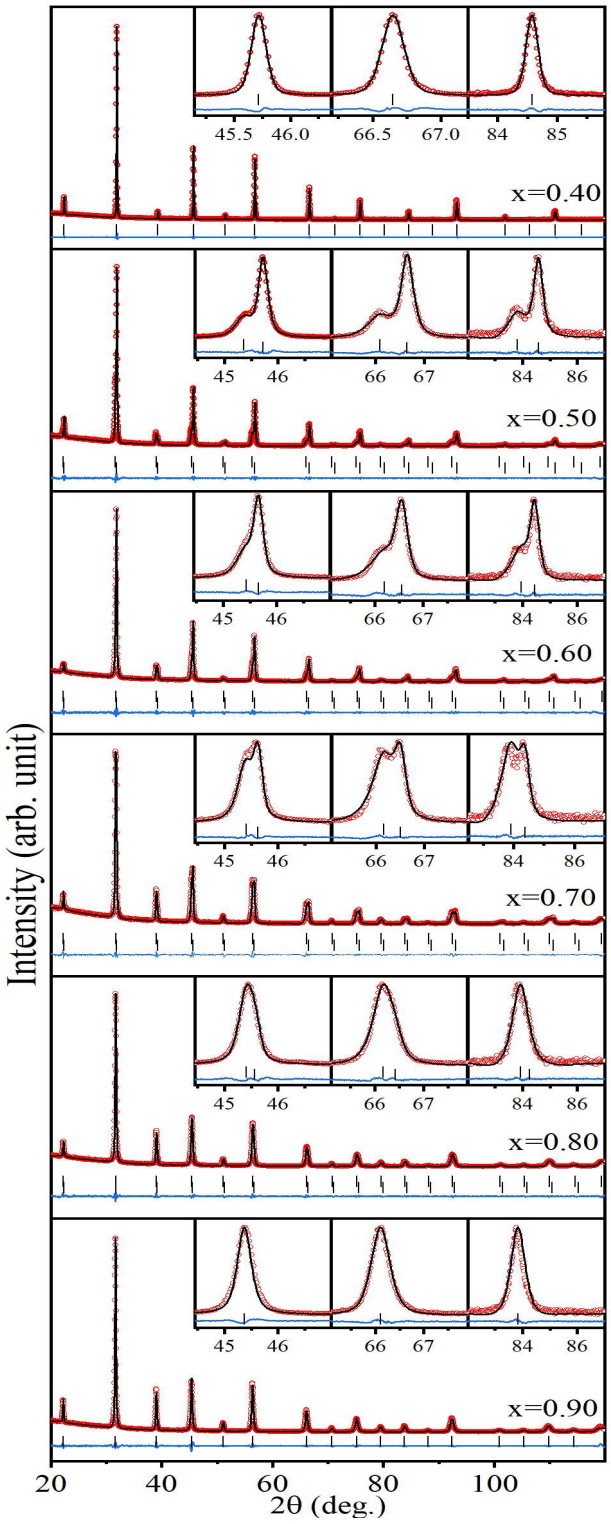

Fig. 3.12 Le-bail Refined X-ray diffraction pattern of NN-xBCT for a few representative compositions. Inset shows the refinement fitting for $\{200\}_{pc}$, $\{220\}_{pc}$, and $\{222\}_{pc}$ perovskite reflections.

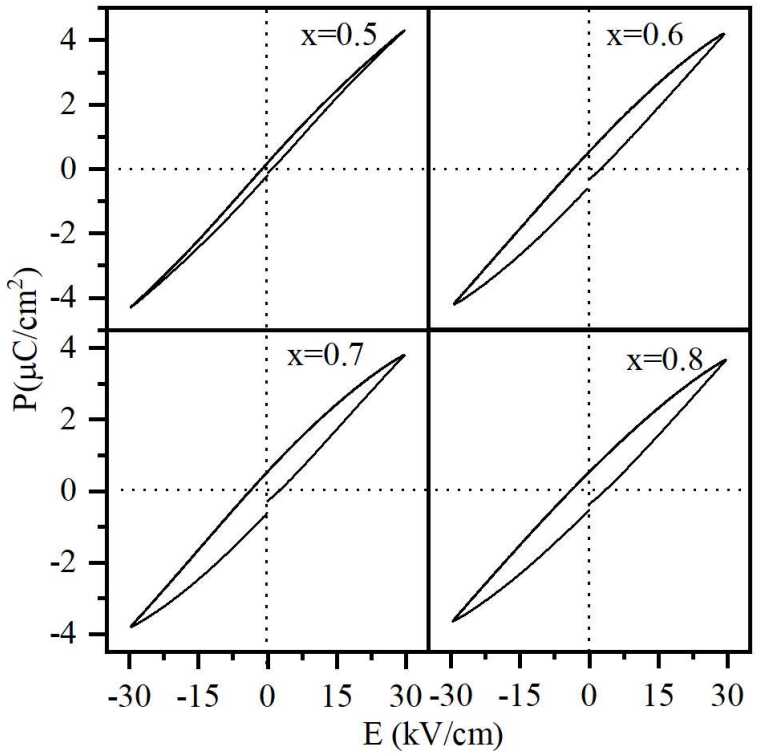

Fig. 3.13 Composition dependent P-E loops for NN-xBCT for $0.50 \leq x \leq 0.80$

cubic model with a $Pm\bar{3}m$ space group as in $x = 0.25$ (hereafter, referred to as C_{NN}). This model fits the diffraction patterns of both compositions very well. However, for $x = 0.50$, a single cubic model was neither sufficient nor reasonable due to the appearance of new reflections at lower angles. The temperature-dependent dielectric curves have their maxima far below the room temperature, suggesting a cubic structure at room temperature (a feature of relaxors). Also, the appearance of new reflections at lower 2θ suggests that the new phase has a larger unit cell volume than the existing one. Therefore, we have tried a two-phase model (both having paraelectric structure), i.e., $Pm\bar{3}m(C_{\mathrm{NN}})$+$Pm\bar{3}m(C_{\mathrm{BT}})$, to fix the diffraction patterns. Here, one cubic phase(C_{NN}) corresponds to Sodium Niobate (smaller unit cell volume), while the other (C_{BT}) corresponds to Barium Titanate (large unit cell volume). The two-phase model (C_{NN}+C_{BT}) was used to fix the structure of all the compositions within the range $0.50 \leq x \leq 0.80$. A single $Pm\bar{3}m$ (C_{BT}) model was

sufficient to fix the diffraction pattern of $x = 0.90$, while a tetragonal model with space group *P4mm* was used to fit the diffraction pattern of $x = 1.0$ (see Fig. 3.12).

Fig. 3.13 illustrates room temperature Polarization-Electric field (P-E) hysteresis loops for compositions with $0.50 \leq x \leq 0.80$ at a frequency of 10 Hz and a field strength of 30 kV/cm. We have observed a slim hysteresis loop suggestive of a non-centrosymmetric crystalline structure, which contradicts the macroscopic cubic phases inferred from X-ray diffraction studies. From the dielectric studies, it becomes clearly evident that the Burns temperature (T_B) for $0.50 \leq x \leq 0.80$ is well above room temperature. As mentioned earlier, below T_B, the polar nanoregions (PNRs) exist in an uncorrelated dynamic state, resulting in a zero time-averaged polarization. Therefore, just below T_B, a hysteresis loop is not expected despite the presence of local polar distortions. Upon further cooling from T_B, an intermediate temperature denoted as T* is defined [130, 134]. Below T*, the correlation among the PNRs starts, their dynamics slow down, and static PNRs become apparent. Consequently, below T*, the system is anticipated to exhibit a slim hysteresis loop, the width of which depends on inter-cluster correlations. Hence, it is clear that the appearance of slim hysteresis loops in a macroscopic cubic matrix for $0.50 \leq x \leq 0.80$ is a result of correlation among the static PNRs also reported in the literature [232, 261]. The presence of polar nanoregions can also influence the intensity of Bragg reflection in the form of diffuse scattering. In the following section, we have used Raman spectroscopy to probe the symmetry of the polar nano regions responsible for the observed high relaxation and slim hysteresis loop for $0.50 \leq x \leq 0.80$.

Raman spectroscopy, due to its sensitivity to local symmetry, is a powerful tool for studying the materials exhibiting local order, including relaxor ferroelectrics characterized by the presence of polar nano regions [247, 262, 263, 264]. The Raman spectrum observed in the relaxor ferroelectrics gives direct evidence of the breakdown of Raman selection rules at the local level [223, 261]. It has been proposed that the symmetry(long-range)

forbidden macroscopic polarization(hysteresis loop) results from the cooperative nature of polar nano regions [261]. The contrasting structural deviations observed in PNRs can not be probed via powder X-ray and neutron diffraction techniques, as they provide us with macroscopic structural information [248]. Fig. 3.14 shows the Raman spectra for NN-xBCT in the composition range $0.30 \leq x \leq 1.0$. The Raman spectra of x=0.30 & 0.40 have four broad bands around 100 cm^{-1} , 220 cm^{-1} , 600 cm^{-1} and 850 cm^{-1}, respectively. This is a common feature of perovskites where broad bands appear due to cationic disorder in a macroscopic cubic matrix [262]. It is important to note that the long-range structure of both compositions is centrosymmetric cubic, and no Raman modes are allowed for this structure. Moreover, for compositions x=0.50 and above, distinctive features emerge. Notably, a new peak at approximately 720 cm^{-1} becomes apparent, particularly in compositions with higher content of the BCT. This particular mode is regarded as a distinct signature of ferroelectricity [223]. It is noteworthy that a similar mode has been observed in Barium Zirconate Titanate (BZT) in its relaxor compositions [223, 265]. Importantly, the local structure in BZT is identified as rhombohedral (*R3m*) through Pair Distribution Function analysis [223]. Moreover, the Raman peak at $\approx$ 600 cm^{-1} gets broadened for x$\geq$0.50 composition, followed by a sharper profile in samples with higher BCT content. Additionally, a novel peak emerges at 305 cm^{-1}, which is a characteristic feature observed in ferroelectric phases of Barium Titanate (BT) and its solid solutions [223, 266, 267]. The presence of a peak at $\approx$ 720 cm^{-1}, a distinct sharp band at approximately 600 cm^{-1}, a peak centered around 305 cm^{-1}, and an interference dip at 123 cm^{-1} collectively suggests the existence of rhombohedral-like clusters within the paraelectric matrix [223, 265]. Therefore, Raman spectroscopy measurements have indicated the presence of local polar order (PNRs) in the macroscopic centrosymmetric matrix. The above-mentioned PNRs are embedded in a long-range non-polar cubic structure and are held responsible for the slim hysteresis loop for $0.40 \leq x \leq 0.80$. In conclusion, the Raman spectra clearly reveal the

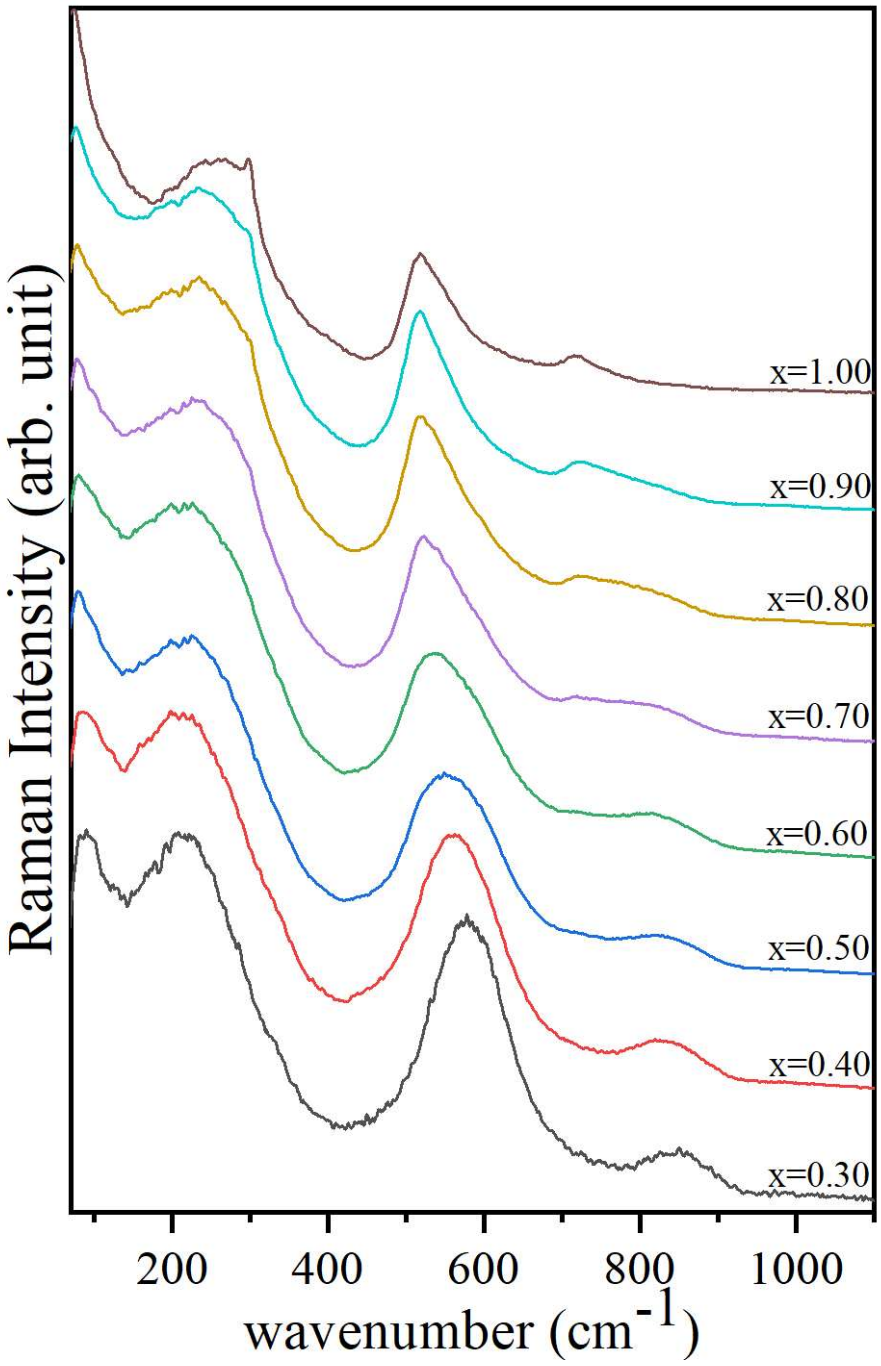

Fig. 3.14 Composition dependent Raman spectra of NN-xBCT for $0.30 \leq x \leq 1.0$

differences between the short and long-range ordering for $0.40 \leq x \leq 0.80$ and the origin of the slim hysteresis loop.

3.4 Conclusion

In conclusion, our study investigates the evolution of crystal structure in the solid solution of (1-x)$NaNbO_3$-$xBa_{0.9}Ca_{0.1}TiO_3$ (NN-xBCT) with varying BCT content (x) using powder X-ray diffraction, temperature-dependent dielectric, and Raman spectroscopic studies. We have identified long-range, crystallographically stable regions as a function of composition using High-resolution X-ray diffraction studies. Antiferroelectric orthorhombic phase of $NaNbO_3$ (SG: *Pbcm*) transforms into a ferroelectric tetragonal phase of $Ba_{0.9}Ca_{0.1}TiO_3$ (SG:*P4mm*) via a series of ferroic phase transitions as follows:
Pbcm [AFE] ($0 \leq x \leq 0.01$) $\rightarrow$ $Pmc2_1$ [FE] ($0.01 \leq x \leq 0.10$) $\rightarrow$ *Amm2* [FE] ($0.08 \leq x \leq 0.15$) $\rightarrow$ *P4bm* [FE] ($0.15 \leq x \leq 0.20$) $\rightarrow$ $Pm\bar{3}m$ (C_{NN}) [PE] ($0.225 \leq x \leq 0.40$) $\rightarrow$ $Pm\bar{3}m$ (C_{NN}) [PE] + $Pm\bar{3}m$ (C_{BT}) [PE] ($0.40 \leq x \leq 0.80$) $\rightarrow$ $Pm\bar{3}m$ (C_{BT}) [PE] (x=0.90) $\rightarrow$ *P4mm* [FE] (x=1.00). These ferroic phases are antiferrodistorted, also possessing ferroelectric order tuned by condensation of zone boundary and zone centre modes *viz.*, $R_4^+(q$ = 1/2,1/2,1/2), M_3^+ (q=1/2,1/2,0), $T_4(q$ = 1/2,1/2,1/4), $\Gamma_4^-(q$ = 0,0,0). For x=0.10, the coexistence of two ferroelectric phases, namely $Pmc2_1$ and *Amm2*, holds special technological significance, suggesting its potential for high electromechanical properties. Further, the temperature-dependent dielectric investigations on x$\geq$0.40 reveal a diffuse and strong frequency dependence of dielectric maxima at low temperatures, indicating the presence of a paraelectric phase at long ranges in ambient conditions. Further, Raman spectroscopic studies on all the compositions reveal the similarities/differences in the structures at short and long ranges. A slim P-E hysteresis loop has been observed for $0.50 \leq x \leq 0.80$ in contrast to the long-range cubic structure. This contrapositive(i.e., hysteresis loop in a centrosymmetric structure) behaviour could be attributed to the correlations

among the polar nano regions exhibiting rhombohedral(*R3m*) symmetry (as confirmed by Raman spectroscopy). These findings provide valuable insights into the long/short-range structure-property correlations and pave the way for potential applications in memory and energy storage devices.

In the subsequent chapters, we have performed a detailed structural analysis of some of the above-mentioned compositions using Synchrotron X-ray diffraction(SXRD), Raman Spectroscopy, and Pair Distribution Function(PDF) analysis in conjunction with dielectric analysis.